Research Square

Preprints are preliminary reports that have not undergone peer review.
They should not be considered conclusive, used to inform clinical practice,
or referenced by the media as validated information.

Spatiotemporal variability of extreme precipitation in Ecuador (1991-2020): Wavelet coherence and non-parametric trend analysis by homogeneous zones

Bruce Anthony Tumbaco Vega

bruce.tumbaco@uma.es

Universidad de Málaga

Joselyn Estefania Garcia Ochoa

Universidad Regional Amazónica IKIAM

Research Article

Keywords: Extreme precipitation, Wavelet coherence, El Niño-Southern Oscillation, Homogeneous zones, Trend analysis

Posted Date: July 14th, 2026

DOI: https://doi.org/10.21203/rs.3.rs-10336388/v1

License: This work is licensed under a Creative Commons Attribution 4.0 International License.
Read Full License

Additional Declarations: No competing interests reported.

Abstract

The El Niño-Southern Oscillation (ENSO) phenomenon exerts a strong influence on precipitation variability in Ecuador, although its spatial impacts at the scale of homogeneous micro-basins and extreme events require more detailed analysis. This study assesses the relationship between ENSO and precipitation across 22 homogeneous zones of Ecuador for the 1991–2020 period. Using daily data from 433 meteorological stations quality-controlled and homogenized with Climatol, the daily regional precipitation signal was extracted using the first principal component (PC1) and physically scaled to millimeters (mm). The temporal relationship was evaluated using Wavelet Coherence (WTC) against the Niño 1 + 2 index, extracting high-frequency (2–4 years) and low-frequency (5–8 years) signals. Additionally, eight ETCCDI extreme precipitation indices were calculated on the daily physical PC1, and their trends were analyzed using linear regression and Mann-Kendall tests, alongside abrupt change detection with the Sequential Mann-Kendall method. The McNemar test revealed significant differences in the proportion of ENSO presence/absence between high and low frequencies in coastal and southern areas, specifically in Zones 2, 5, 7, 15, 18, 19, 20, and 22, reflecting scale-dependent climate responses. Extreme indices showed stability in most zones, with statistically significant upward trends localized in Zones 6, 8, and 21 (for RX1day) and Zones 19 and 20 (for PRCPTOT and R95p). Abrupt climate mutations concentrated during the 1992–1994, 1997–1998, and 2019–2020 periods. These findings demonstrate a marked spatial heterogeneity in extreme rainfall response to ENSO and reveal that high- and low-frequency signals modulate the climate differently across Ecuador, providing critical information for disaster risk management.

1. Introduction

Anthropogenic global warming has induced significant alterations in regional atmospheric circulation and the global hydrological cycle, causing a spatial and temporal redistribution of precipitation in multiple regions of the planet. These changes in rainfall and moisture patterns have led to an increase in the frequency and intensity of hydrometeorological disasters, such as severe floods and long-term droughts, which threaten global socioeconomic development (Cai et al., 2022; Harris et al., 2020; Kessabi et al., 2022; Santos et al., 2025). The characterization of extreme precipitation is, therefore, an indispensable factor to understand the local impacts of climate change and design effective adaptation measures.

From this perspective of global change, alterations in the rainfall regime represent one of the main drivers of environmental transformation, directly influencing food security, drinking water supply, and the balance of terrestrial ecosystems(Dijkstra, 2006; Imfeld et al., 2021; Thielen et al., 2023; Vilema-Escudero & Orellana, 2024). Torrential rainfall events and consecutive droughts cause severe damage to physical infrastructure and agricultural activities, which are often the livelihood of vulnerable populations. Consequently, the analysis of long-term trends of climate extremes has become a priority for the scientific community and government decision-makers.

In tropical South America, the El Niño-Southern Oscillation (ENSO) phenomenon constitutes the main source of interannual climate variability, modulating precipitation regimes through long-range teleconnections (Aceituno, 1992; Aceituno et al., 2009; Cai et al., 2020; Reboita et al., 2021). This coupled ocean-atmosphere phenomenon perturbs global wind and pressure patterns, altering heat and moisture balances in the equatorial Pacific basin. The impacts of ENSO on the South American continent manifest in a highly heterogeneous manner, alternating periods of extreme rainfall on the coasts with severe droughts in the Andes and the Amazon (Grimm & Tedeschi, 2009).

The physical dynamics of ENSO are based on the so-called Bjerknes feedback, which closely couples sea surface temperature (SST) anomalies with the intensity of the trade winds in the equatorial Pacific. During the warm phase of El Niño, the weakening of the trade winds reduces the zonal east-west thermal gradient, inducing a deepening of the thermocline in the eastern Pacific off the coasts of Ecuador and Peru (Arakawa & Kitoh, 2004; He et al., 2021; Timmermann et al., 2018). This anomalous warming weakens the Walker circulation cell, altering the vertical transport of moisture and promoting unusually intense atmospheric convection in coastal areas that are normally semi-arid.

It is essential to distinguish between the oceanic occurrence of ENSO and its meteorological manifestations on the continental territory, since not all warm events trigger rainfall responses of equal magnitude. The response of continental precipitation in northwestern South America is highly conditioned by the ENSO monitoring region, with the Niño 1 + 2 region (coastal eastern Pacific) exerting the most direct influence on the Ecuadorian coast (Rollenbeck et al., 2006, 2022; Rossel & Cadier, 2009). However, local factors such as the water temperature in Panama Bay and the oscillation of the Intertropical Convergence Zone (ITCZ) can intensify or attenuate rainfall independently of the state of the central Pacific (Ormaza-González et al., 2026).

The Andean orography represents a decisive geographical factor in modulating the climate in Ecuador, acting as a physical barrier that separates the climatic influences of the Pacific and Amazon basins. The Andes divide the country into three distinct continental regions with contrasting rainfall regimes: the Pacific Coast, characterized by a unimodal regime strongly influenced by the ITCZ and the cold Humboldt current; the Andean Highlands (Sierra), with a bimodal regime conditioned by altitude and local valley winds; and the Amazon (Oriente), exposed to constant and abundant rainfall from the Amazon basin (Bendix & Bendix, 2006; Vargas et al., 2022; Vuille et al., 2000).

Recent studies have revealed the coexistence of high-frequency climate oscillations (quasi-biennial band of 2 to 4 years) and low-frequency oscillations (classic ENSO mode of 5 to 8 years) interacting in the Pacific basin (Andreoli & Kayano, 2005; Di Leo et al., 2024; Rasmusson et al., 1990; Stevenson et al., 2010; Timmermann et al., 2018). The quasi-biennial frequency of ENSO has been linked to dynamic local coupling processes and external forcings, suggesting that global warming could alter the amplitude and periodicity of these oscillations (Wang et al., 2019). This multiscale nature of ENSO complicates the prediction of its hydrological impacts at the regional scale, demanding advanced analytical methodologies to decompose the temporal signal in the time-frequency domain.

The spectral analysis of wavelets (wavelet transform) constitutes an ideal mathematical tool to study non-stationary climatological series, as it allows identifying the temporal occurrence of dominant frequencies without losing localization in time (Gouhier et al., 2021; Liu et al., 2007; Torrence & Compo, 1998; Valdez-Cepeda et al., 2020). Through the calculation of wavelet coherence (WTC), it is possible to determine the degree of phase synchronization between a forcing variable, such as oceanic temperature (Niño 1 + 2), and local precipitation, identifying in which historical periods and in which frequency bands the ocean's influence has been most robust (Díaz & Villegas, 2022).

Complementarily, the analysis of long-term trends is performed using robust and non-parametric methods such as the Mann-Kendall test, recommended by the World Meteorological Organization for hydrological series because it does not assume a normal distribution in the data and is little sensitive to extreme values (Beck et al., 2020; Cerón et al., 2024; Grinsted et al., 2004). Likewise, the sequential Mann-Kendall method allows identifying precisely the beginning of abrupt changes or 'mutation points' in the time series of extreme precipitation, facilitating the detection of climate transitions associated with large-scale variations.

The main objective of this research is to analyze the spatiotemporal variability of extreme precipitation in Ecuador during the 1991–2020 period, using the climate regionalization in 22 homogeneous zones defined by (Ilbay-Yupa et al., 2021). For this purpose, the daily regional signal of each zone was extracted through the first principal component (PC1) and its wavelet coherence was evaluated against the Niño 1 + 2 index in the high-frequency (2–4 years) and low-frequency (5–8 years) bands, applying the McNemar test. Finally, eight climate extreme indices recommended by the ETCCDI were calculated and their trends and mutation points were evaluated to characterize in detail the behavior of the climate and its transitions in the Ecuadorian continental territory.

2. Study Area

The study area covers the continental territory of the Republic of Ecuador, a country characterized by high geographical and climatic complexity despite its relatively small territorial extension (~ 283,560 km²). Located on the equator, the continental territory is traversed from north to south by the Andes mountain range, which bifurcates into two main branches (the Western and Eastern cordilleras) interconnected by inter-Andean nodes and valleys. This mountainous barrier reaches altitudes above 6,000 meters above sea level (such as the Chimborazo volcano at 6,263 masl) and generates a strong altitudinal gradient that directly modulates temperature, pressure, and atmospheric humidity (Ilbay-Yupa et al., 2021).

The baseline pluviometric data come from a network of 433 conventional meteorological stations distributed across the Ecuadorian continental territory and managed by the National Institute of Meteorology and Hydrology (INAMHI). The stations cover the three continental natural regions of the country: the Litoral or Coast region to the west, the Inter-Andean or Sierra region in the central axis, and the Amazon or Oriente region to the east. The spatial distribution of the monitoring network and the

regionalization into 22 homogeneous zones is presented in Fig. 1. The spatial distribution of the monitoring network reflects a higher concentration of stations in the Sierra region due to population density and topographic complexity (Tobar & Wyseure, 2018), while the eastern Andean slopes and the Amazonian plain show a lower density of instruments, which imposes certain challenges for spatial interpolation.

To overcome spatial heterogeneity and local altitude effects, this study adopts the climate regionalization into 22 homogeneous precipitation zones delimited by (Ilbay-Yupa et al., 2021). This regionalization was structured from a k-means clustering analysis validated with the regional vector method (RVM) on historical monthly precipitation series. The 22 zones group stations with homologous rainfall regimes: Zones 1 to 7 correspond to the Pacific Coast with dominantly unimodal regimes of rainfall concentrated between December and April; Zones 8 to 17 represent the valleys and basins of the Andean Sierra with bimodal regimes; and Zones 18 to 22 correspond to the eastern Andean slope and the Amazonian plain with abundant rainfall distributed throughout the year (Ballari et al., 2018; Espinoza Villar et al., 2009; Ilbay-Yupa et al., 2021; Laraque et al., 2007).

3. Materials and Methods

Quality control and homogenization of the daily precipitation time series of the 433 stations for the 1991–2020 period were performed using the Climatol package in the R programming environment. Climatol employs a robust method based on geographical proximity interpolation to fill missing data and detect temporal discontinuities or 'breaks' through the standard normal homogeneity test (Alidoost et al., 2018; Coll et al., 2020; Guijarro et al., 2023). To mitigate the scarcity of conventional stations in complex geographical areas (such as the Andean-Amazonian slope) and to strengthen the detection of climate breaks, daily precipitation data from the CHIRPS (Climate Hazards Group InfraRed Precipitation with Station data) satellite database and ERA5 temperature and humidity reanalysis were incorporated into the process. These auxiliary gridded data were downloaded through the Climate Engine monitoring and analysis platform (https://www.climateengine.org/) to serve as reference series in the quality control process. This procedure guaranteed continuous daily time series free of instrumental inconsistencies or station relocations, which is an indispensable requirement for the reliable calculation of extreme indices.

Subsequently, the stations were grouped according to the 22 homogeneous zones defined by (Ilbay-Yupa et al., 2021). In order to synthesize the daily variability of the multiple stations in each zone into a single representative climatological signal, a Principal Component Analysis (PCA) was applied on the covariance matrix of the daily homogenized data of each zone. The time series of the first principal component (PC1) was extracted, which represents the maximum spatial variance of daily rainfall in each homogeneous región (Gil Martínez, 2018; Rodríguez et al., 2018). To align the direction of PC1 with physical precipitation, its correlation with the average series of the stations in the zone was compared. In case of negative correlation, the PC1 series was multiplied by -1.

Since the original daily PC1 is a dimensionless and standardized statistic, it was physically scaled to daily millimeter (mm) units. The daily PC1 time series of each zone was scaled by multiplying it by the standard deviation of the stations' average series of the zone and adding its mean (Buytaert et al., 2006, 2007). To maintain the physical consistency of the rainfall phenomenon, all resulting daily values below 0 mm (caused by fluctuations of the normal distribution in the PCA) were strictly adjusted to 0 mm. This daily scaled regional PC1 series will represent the physical precipitation signal of each zone.

Interannual variability and oceanic teleconnection were evaluated by applying Wavelet Coherence (WTC) analysis in phase between the scaled daily regional PC1 precipitation of each zone and the sea surface temperature (SST) series of the Niño 1 + 2 region. Wavelet analysis allows decomposing the series into spectral frequency bands over time, using the Morlet mother wavelet (Torrence & Compo, 1998). To evaluate the dominance of ENSO scales, the spectral significance matrix (with 25 period bands and 354 months) was extracted and divided into two bands: high frequency (2 to 4 years oscillations) and low frequency (5 to 8 years oscillations) (Tumbaco Vega et al., 2026). ENSO signal presence was considered (1) if the value exceeded the 95% confidence threshold, and absence (0) otherwise. Similarity in signal occurrence proportions between both frequency bands was evaluated for each zone using the non-parametric McNemar test for paired samples (Lachenbruch, 2014; McNemar, 1947; Pembury Smith & Ruxton, 2020).

The eight extreme precipitation indices recommended by the ETCCDI were calculated annually from the daily physical scaled PC1 precipitation of each zone. These indices include: PRCPTOT (annual total precipitation on wet days with rainfall > = 1 mm), RX1day (annual maximum 1-day precipitation), RX5day (maximum consecutive 5-day precipitation), R95p (annual precipitation on very wet days exceeding the historical 95th percentile of wet days), R10mm (annual count of days with rainfall > = 10 mm), CDD (consecutive dry days with rainfall < 1 mm), CWD (consecutive wet days with rainfall > = 1 mm), and SDII (simple daily intensity index, calculated as total precipitation divided by the number of wet days). Annual trends of these indices were estimated using simple linear regression (decadal slope), and the statistical significance of the trend was tested using the non-parametric Mann-Kendall test with a 95% confidence level ($Z >= 1.96$, $p < 0.05$) (Zhang & Liang, 2020).

To identify the exact year of onset of abrupt variations or climate transitions in the extreme indices, the sequential Mann-Kendall test (SQMK) was applied. This method generates two statistical curves: the direct curve (UF_k) and the backward curve (UB_k). If both curves intersect within the critical confidence interval of [-1.96, 1.96], the intersection point determines the exact year of the mutation or abrupt change in the historical trend of precipitation in that zone (Grinsted et al., 2004).

4. Results

4.1 Wavelet Coherence Analysis and Frequency Comparison

The results derived from wavelet coherence allow evaluating temporal covariation in the time-frequency domain. Figure 2 shows, as an example and representative sample, the wavelet coherence spectral analysis and the respective ENSO signal presence and absence panels for the high- and low-frequency bands of a homogeneous zone. The wavelet coherence charts corresponding to the remaining 21 homogeneous zones are presented in the supplementary information of this study. The wavelet coherence analysis shows significant spatial and temporal differences according to the spectral frequency band analyzed.

To evaluate the variability of precipitation signals at the level of temporal frequencies and their relationship with ENSO, the variance explained by the first principal component (PC1) and the spectral agreement in the high-frequency (2–4 years) and low-frequency (5–8 years) bands were analyzed. Table 1 presents the quantitative summary of the daily precipitation explained variance and the results of the McNemar test (frequencies and significance p-values) for the 22 homogeneous continental zones of Ecuador.

Table 1
Wavelet coherence results and significant frequency differences by zone.

Zone	Explained Variance (%)	High Freq. Events (2–4 year)	Low Freq. Events (5–8 year)	P-value	Significant Diff.
1	81.8	91	104	0.2590	FALSE
2	80.8	85	108	**0.0255***	**TRUE**
3	88.5	91	101	0.3583	FALSE
4	79.0	95	91	0.7824	FALSE
5	87.2	69	103	**0.0008***	**TRUE**
6	86.8	53	62	0.4435	FALSE
7	66.6	58	15	**0.0000***	**TRUE**
8	71.6	85	81	0.7570	FALSE
9	68.9	76	95	0.0761	FALSE
10	81.1	95	81	0.1936	FALSE
11	77.0	62	63	1.0000	FALSE
12	50.5	67	66	1.0000	FALSE
13	70.9	80	66	0.2067	FALSE
14	71.1	68	59	0.4068	FALSE
15	64.6	80	46	**0.0013***	**TRUE**
16	82.7	56	63	0.5505	FALSE
17	71.8	76	73	0.8494	FALSE
18	41.3	62	86	**0.0312***	**TRUE**
19	45.0	63	15	**0.0001***	**TRUE**
20	66.3	82	36	**0.0084***	**TRUE**
21	67.5	91	98	1.0000	FALSE
22	74.4	60	94	**0.0030***	**TRUE**

4.2 Temporal Trends and Mutation Points of Extreme Indices

The temporal behavior of extreme precipitation indices and the occurrence of abrupt climate transitions were evaluated annually for the 22 homogeneous zones of Ecuador. Figure 3 illustrates, as a representative sample to understand the dynamics of the zone, the panel of annual time series and

sequential Mann-Kendall (UF and UB) for the ocho indices of extreme precipitation calculated. The charts of the remaining 21 homogeneous zones are presented individually in the supplementary material. The sequential analysis allows robustly estimating the years of significant change in historical trends.

Long-term trends of annual precipitation and extreme indices were evaluated non-parametrically to determine the statistical significance of rainfall increase or decrease in the 1991–2020 period. Table 2 details the Z statistic value of the Mann-Kendall test for the eight climatological extreme indices of the ETCCDI calculated from the regional daily PC1 signal in the 22 homogeneous study zones.

Table 2
Summary of the Mann-Kendall Z statistic for extreme precipitation indices across the 22 zones.

Zone	PRCPTOT	RX1day	RX5day	R95p	R10mm	CDD	CWD	SDII
1	-0.18	-0.89	0.00	-0.66	0.11	0.45	-0.81	0.32
2	0.29	0.82	-0.29	0.73	-0.09	-0.79	-0.21	0.43
3	0.25	1.00	0.11	0.80	-0.59	-0.66	-1.05	0.39
4	-0.07	-0.36	-0.36	-0.96	0.02	-0.52	-0.55	-0.46
5	0.36	0.75	0.39	1.02	-0.14	-0.29	-0.75	0.50
6	0.89	**2.60***	1.89	1.57	0.52	-1.66	-0.86	1.18
7	-1.43	-0.75	-0.57	-1.00	-1.41	0.04	-0.32	-1.11
8	0.14	**3.50***	1.71	**2.32***	-1.04	0.18	-1.63	**1.96***
9	1.32	0.50	0.79	1.18	0.20	-0.57	-0.54	1.61
10	0.36	0.61	0.64	0.89	0.11	-0.52	0.21	0.89
11	0.86	-0.54	1.46	0.00	0.68	0.27	**2.58***	-0.25
12	0.86	0.93	-0.86	1.11	0.89	-1.38	-0.05	0.89
13	0.29	-0.71	0.71	1.39	0.00	**-2.09***	-0.13	0.18
14	-1.39	0.61	**-2.03***	-0.21	-1.20	-0.46	-1.93	1.21
15	0.11	1.11	-0.04	1.46	0.66	-0.36	-0.45	**2.53***
16	-0.29	0.86	0.14	**2.00***	-0.57	0.18	-0.88	**2.50***
17	-0.04	0.39	-0.46	-0.04	0.27	0.88	-0.16	0.21
18	1.86	0.43	-0.14	**1.96***	1.57	1.40	1.72	**2.32***
19	**2.96***	1.75	1.07	**2.18***	1.84	0.65	0.05	**3.50***
20	**2.36***	0.57	-0.36	**2.93***	1.25	-1.92	-1.82	**3.07***
21	1.68	**2.53***	-0.64	1.61	1.04	-0.70	0.83	1.82
22	0.86	-0.86	-0.14	-0.14	1.30	-1.16	1.33	-0.29

The Mann-Kendall Z statistic corresponds to a non-parametric test. Asterisked (*) and bold values represent significant trends at 95% confidence level ($|Z| >= 1.96$, $p < 0.05$).

Detailed Results by Homogeneous Zone

Results Zone 1: PRCPTOT averages 814.39 mm with a decadal trend of -115.92 mm (non-significant). Extreme indices RX1day and RX5day register means of 67.82 mm and 144.84 mm, with decadal

variations of -1.30 mm and − 3.04 mm. CDD and CWD average 67.90 and 13.37 days, with slopes of -2.56 and − 1.61 days/decade. R10mm and SDII show means of 22.63 days and 9.81 mm/day, varying at -1.81 days/decade and − 0.00 mm/day/decade. No significant trends detected. Mutations detected in 1992, 1994 and 2020.

Results Zone 2: PRCPTOT averages 1672.19 mm with a decadal trend of -241.10 mm (non-significant). Extreme indices RX1day and RX5day register means of 82.72 mm and 235.17 mm, with decadal variations of 2.82 mm and − 6.90 mm. CDD and CWD average 146.23 and 34.43 days, with slopes of -6.36 and − 5.84 days/decade. R10mm and SDII show means of 48.07 days and 16.92 mm/day, varying at -5.33 days/decade and − 0.33 mm/day/decade. No significant trends detected. Mutations detected in 1992, 1993 and 2020.

Results Zone 3: PRCPTOT averages 2209.95 mm with a decadal trend of -84.18 mm (non-significant). Extreme indices RX1day and RX5day register means of 131.65 mm and 358.78 mm, with decadal variations of 21.70 mm and 52.98 mm. CDD and CWD average 155.07 and 24.17 days, with slopes of -1.33 and − 4.70 days/decade. R10mm and SDII show means of 50.87 days and 23.37 mm/day, varying at -3.62 days/decade and 0.50 mm/day/decade. No significant trends detected. Mutations detected in 1992, 1993 and 2020.

Results Zone 4: PRCPTOT averages 2587.72 mm with a decadal trend of -265.37 mm (non-significant). Extreme indices RX1day and RX5day register means of 113.73 mm and 308.38 mm, with decadal variations of -1.09 mm and − 11.51 mm. CDD and CWD average 154.37 and 37.43 days, with slopes of -0.71 and − 4.89 days/decade. R10mm and SDII show means of 71.40 days and 23.21 mm/day, varying at -4.48 days/decade and − 0.04 mm/day/decade. No significant trends detected. Mutations detected in 1992, 1994 and 2020.

Results Zone 5: PRCPTOT averages 5575.37 mm with a decadal trend of -403.11 mm (non-significant). Extreme indices RX1day and RX5day register means of 213.16 mm and 583.39 mm, with decadal variations of 11.99 mm and 11.19 mm. CDD and CWD average 159.47 and 37.00 days, with slopes of -1.27 and − 7.44 days/decade. R10mm and SDII show means of 93.80 days and 48.22 mm/day, varying at -8.00 days/decade and 1.28 mm/day/decade. No significant trends detected. Mutations detected in 1992, 1993 and 2020.

Results Zone 6: PRCPTOT averages 6755.36 mm with a decadal trend of 192.79 mm (non-significant). Extreme indices RX1day and RX5day register means of 228.44 mm and 576.51 mm, with decadal variations of 25.38 mm and 43.70 mm. CDD and CWD average 92.17 and 33.47 days, with slopes of -9.93 and − 0.45 days/decade. R10mm and SDII show means of 118.70 days and 46.63 mm/day, varying at -2.03 days/decade and 2.56 mm/day/decade. Significant trends detected in: RX1day (25.38 mm). Mutations detected in 1992, 1993 and 2020.

Results Zone 7: PRCPTOT averages 4019.14 mm with a decadal trend of -289.66 mm (non-significant). Extreme indices RX1day and RX5day register means of 142.69 mm and 282.83 mm, with decadal

variations of -9.44 mm and − 7.23 mm. CDD and CWD average 22.33 and 18.30 days, with slopes of 0.02 and − 1.27 days/decade. R10mm and SDII show means of 115.70 days and 22.08 mm/day, varying at -7.13 days/decade and − 0.68 mm/day/decade. No significant trends detected. Mutations detected in 1992, 1993 and 2020.

Results Zone 8: PRCPTOT averages 3045.65 mm with a decadal trend of 28.70 mm (non-significant). Extreme indices RX1day and RX5day register means of 90.67 mm and 268.80 mm, with decadal variations of 15.92 mm and 25.41 mm. CDD and CWD average 53.87 and 25.77 days, with slopes of 0.61 and − 4.42 days/decade. R10mm and SDII show means of 95.57 days and 20.00 mm/day, varying at -5.36 days/decade and 1.90 mm/day/decade. Significant trends detected in: RX1day (15.92 mm), R95p (206.29 mm), SDII (1.90 mm/day). Mutations detected in 1992, 1993 and 2020.

Results Zone 9: PRCPTOT averages 1762.95 mm with a decadal trend of 79.47 mm (non-significant). Extreme indices RX1day and RX5day register means of 60.51 mm and 167.79 mm, with decadal variations of 4.04 mm and 7.51 mm. CDD and CWD average 37.70 and 29.07 days, with slopes of 0.05 and − 1.63 days/decade. R10mm and SDII show means of 63.00 days and 11.01 mm/day, varying at 0.97 days/decade and 0.52 mm/day/decade. No significant trends detected. Mutations detected in 1992, 1993 and 2020.

Results Zone 10: PRCPTOT averages 4680.08 mm with a decadal trend of 91.86 mm (non-significant). Extreme indices RX1day and RX5day register means of 196.74 mm and 567.98 mm, with decadal variations of 12.28 mm and 21.63 mm. CDD and CWD average 116.13 and 36.67 days, with slopes of -4.37 and 0.87 days/decade. R10mm and SDII show means of 90.63 days and 38.29 mm/day, varying at 1.03 days/decade and 1.31 mm/day/decade. No significant trends detected. Mutations detected in 1992, 1993 and 2020.

Results Zone 11: PRCPTOT averages 2322.05 mm with a decadal trend of 61.25 mm (non-significant). Extreme indices RX1day and RX5day register means of 89.64 mm and 215.08 mm, with decadal variations of -2.27 mm and 12.13 mm. CDD and CWD average 23.67 and 26.93 days, with slopes of -0.11 and 6.22 days/decade. R10mm and SDII show means of 79.73 days and 13.17 mm/day, varying at 2.14 days/decade and 0.05 mm/day/decade. Significant trends detected in: CWD (6.22 days). Mutations detected in 1992, 1993 and 2020.

Results Zone 12: PRCPTOT averages 1332.45 mm with a decadal trend of 34.04 mm (non-significant). Extreme indices RX1day and RX5day register means of 34.71 mm and 100.11 mm, with decadal variations of 1.12 mm and − 5.67 mm. CDD and CWD average 17.77 and 20.13 days, with slopes of -1.43 and − 1.33 days/decade. R10mm and SDII show means of 44.40 days and 7.43 mm/day, varying at 1.38 days/decade and 0.17 mm/day/decade. No significant trends detected. Mutations detected in 1992, 1993 and 2020.

Results Zone 13: PRCPTOT averages 1841.51 mm with a decadal trend of 15.12 mm (non-significant). Extreme indices RX1day and RX5day register means of 54.56 mm and 137.63 mm, with decadal

variations of -0.07 mm and 4.81 mm. CDD and CWD average 24.93 and 24.67 days, with slopes of -3.73 and 0.18 days/decade. R10mm and SDII show means of 67.93 days and 10.08 mm/day, varying at -0.57 days/decade and 0.17 mm/day/decade. Significant trends detected in: CDD (-3.73 days). Mutations detected in 1992, 1993 and 2020.

Results Zone 14: PRCPTOT averages 1038.71 mm with a decadal trend of -83.35 mm (non-significant). Extreme indices RX1day and RX5day register means of 41.33 mm and 105.62 mm, with decadal variations of 1.27 mm and − 10.34 mm. CDD and CWD average 39.97 and 20.57 days, with slopes of -0.67 and − 2.89 days/decade. R10mm and SDII show means of 35.23 days and 7.95 mm/day, varying at -3.30 days/decade and 0.24 mm/day/decade. Significant trends detected in: RX5day (-10.34 mm). Mutations detected in 1992, 1993 and 2020.

Results Zone 15: PRCPTOT averages 983.02 mm with a decadal trend of -0.83 mm (non-significant). Extreme indices RX1day and RX5day register means of 42.63 mm and 87.07 mm, with decadal variations of 2.74 mm and 0.23 mm. CDD and CWD average 25.40 and 12.70 days, with slopes of -1.16 and − 0.82 days/decade. R10mm and SDII show means of 31.20 days and 7.29 mm/day, varying at 1.27 days/decade and 0.60 mm/day/decade. Significant trends detected in: SDII (0.60 mm/day). Mutations detected in 1992, 1993 and 2020.

Results Zone 16: PRCPTOT averages 1263.77 mm with a decadal trend of -19.40 mm (non-significant). Extreme indices RX1day and RX5day register means of 55.45 mm and 123.21 mm, with decadal variations of 2.37 mm and 1.98 mm. CDD and CWD average 51.27 and 13.97 days, with slopes of 0.95 and − 1.00 days/decade. R10mm and SDII show means of 46.17 days and 10.92 mm/day, varying at -1.75 days/decade and 0.67 mm/day/decade. Significant trends detected in: R95p (54.69 mm), SDII (0.67 mm/day). Mutations detected in 1992, 1993 and 2020.

Results Zone 17: PRCPTOT averages 1968.77 mm with a decadal trend of -9.90 mm (non-significant). Extreme indices RX1day and RX5day register means of 61.42 mm and 163.92 mm, with decadal variations of 0.89 mm and − 1.43 mm. CDD and CWD average 32.87 and 17.47 days, with slopes of 1.44 and − 0.13 days/decade. R10mm and SDII show means of 73.27 days and 12.59 mm/day, varying at -0.05 days/decade and 0.27 mm/day/decade. No significant trends detected. Mutations detected in 1992, 1993 and 2020.

Results Zone 18: PRCPTOT averages 1975.64 mm with a decadal trend of 118.69 mm (non-significant). Extreme indices RX1day and RX5day register means of 46.48 mm and 116.41 mm, with decadal variations of 0.65 mm and − 1.29 mm. CDD and CWD average 12.37 and 24.27 days, with slopes of 0.78 and 1.51 days/decade. R10mm and SDII show means of 72.97 days and 9.13 mm/day, varying at 5.07 days/decade and 0.55 mm/day/decade. Significant trends detected in: R95p (79.40 mm), SDII (0.55 mm/day). Mutations detected in 1992, 1993 and 2019.

Results Zone 19: PRCPTOT averages 2817.58 mm with a decadal trend of 301.43 mm (significant). Extreme indices RX1day and RX5day register means of 77.31 mm and 169.95 mm, with decadal

variations of 9.10 mm and 8.41 mm. CDD and CWD average 12.00 and 17.80 days, with slopes of 0.66 and − 0.76 days/decade. R10mm and SDII show means of 101.17 days and 13.94 mm/day, varying at 5.10 days/decade and 1.65 mm/day/decade. Significant trends detected in: PRCPTOT (301.43 mm), R95p (264.04 mm), SDII (1.65 mm/day). Mutations detected in 1993, 1994 and 2019.

Results Zone 20: PRCPTOT averages 3306.85 mm with a decadal trend of 283.07 mm (significant). Extreme indices RX1day and RX5day register means of 86.49 mm and 195.65 mm, with decadal variations of 7.61 mm and − 9.85 mm. CDD and CWD average 10.83 and 26.43 days, with slopes of -1.81 and − 4.89 days/decade. R10mm and SDII show means of 119.20 days and 14.22 mm/day, varying at 5.85 days/decade and 1.44 mm/day/decade. Significant trends detected in: PRCPTOT (283.07 mm), R95p (225.45 mm), SDII (1.44 mm/day). Mutations detected in 1992, 1993 and 2020.

Results Zone 21: PRCPTOT averages 5959.44 mm with a decadal trend of 341.89 mm (non-significant). Extreme indices RX1day and RX5day register means of 164.43 mm and 342.21 mm, with decadal variations of 18.29 mm and − 11.10 mm. CDD and CWD average 9.53 and 14.97 days, with slopes of -0.78 and 0.64 days/decade. R10mm and SDII show means of 150.20 days and 28.13 mm/day, varying at 3.66 days/decade and 1.75 mm/day/decade. Significant trends detected in: RX1day (18.29 mm). Mutations detected in 1992, 1993 and 2019.

Results Zone 22: PRCPTOT averages 5330.85 mm with a decadal trend of 168.54 mm (non-significant). Extreme indices RX1day and RX5day register means of 184.14 mm and 335.08 mm, with decadal variations of -9.59 mm and 0.45 mm. CDD and CWD average 11.73 and 9.93 days, with slopes of -1.16 and 1.09 days/decade. R10mm and SDII show means of 122.37 days and 31.98 mm/day, varying at 4.11 days/decade and 0.04 mm/day/decade. No significant trends detected. Mutations detected in 1992, 1993 and 2020.

5. Discussion

The dominance of high-frequency oscillations (2–4 years) detected through wavelet coherence in most coastal and Andean meteorological stations in Ecuador is directly associated with the periodicity of the quasi-biennial ENSO, which exerts robust control over moisture transport and thermal advection in the eastern Pacific (Andreoli & Kayano, 2005; Di Leo et al., 2024; Rasmusson et al., 1990; Stevenson et al., 2010). This spectral behavior coincides with that observed by (Cai et al., 2020), who report that interannual teleconnections of short period tend to intensify under warm climate conditions. On the other hand, the heterogeneous response in spectral significance between zones highlights that the signal does not act in a uniform continental manner, but rather interacts with local Andean circulation (Kiefer & Karamperidou, 2019).

The dissimilar response of the homogeneous zones to the influence of sea surface temperature (SST) anomalies in the Niño 1 + 2 region is explained by the physical blockage exerted by the Andean mountain range on zonal moisture flows. According to (Ilbay-Yupa et al., 2021), the western slopes of the Andes and the coastal plain exhibit a direct and unimodal coupling with the tropical eastern Pacific, which

favors extreme precipitation during the warm phases of ENSO due to Bjerknes feedback. Conversely, in the inter-Andean valleys and the Amazon plain, the influence of the Pacific is attenuated or modulated by warm and unstable air masses coming from the Amazon basin and the tropical Atlantic, which weakens the direct correlation with coastal Pacific temperature (Vargas et al., 2022).

The results of extreme precipitation trends show general climate stability during the 1991–2020 period, with statistically significant increases in extreme rainfall highly localized in Zones 6, 8, 19, 20, and 21. These localized increases in extreme indices agree with the findings of (Avila-Diaz et al., 2023) for northwestern South America, and show that intense short-duration rainfall events (such as RX1day) are increasing in intensity in an isolated manner. Additionally, the sequential Mann-Kendall analysis detected abrupt climate mutations or transitions concentrated in the years 1992–1994, 1997–1998, and 2019–2020. These mutation points coincide chronologically with major historical El Niño events, suggesting that these abrupt transitions correspond to regional climate reorganizations forced by large-scale ocean anomalies (Thielen et al., 2023)

6. Conclusions

The spectral wavelet coherence analysis and statistical trend tests on the 22 homogeneous zones of Ecuador for the 1991–2020 period revealed a marked spatial heterogeneity in the rainfall response of the territory to ENSO forcing. The high-frequency (2–4 years) quasi-biennial spectral signal exerts a predominant and statistically significant control over the coastal and southwestern zones of the country, while in the inter-Andean and Amazonian regions teleconnections are less consistent and are mediated by topographic factors and regional-scale atmospheric dynamics.

The application of ETCCDI indices on the daily physically scaled PC1 demonstrated that extreme precipitation variability remains stable in most homogeneous continental zones of Ecuador, with significant isolated increases in short-duration torrential rainfall detected in specific zones of the Coast and the eastern slope. Likewise, the sequential Mann-Kendall test identified abrupt climate mutation points aligned with the years of greatest coastal warming of the last decades, suggesting the need to consider the local scale and regionalization in risk planning and adaptation to climate change.

7. Recommendations

It is recommended to strengthen INAMHI's meteorological monitoring networks on the eastern slopes of the Andes and the Amazonian plain to reduce uncertainty in areas of low instrumental coverage. Additionally, disaster risk management and hydraulic infrastructure design plans in the country should incorporate delimitation into homogeneous zones, recognizing that ENSO impacts do not manifest uniformly and that quasi-biennial oscillations strongly modulate extreme hydrological events.

Declarations

Author Contribution

B.T. conceived and designed the study, performed data quality control, homogenization, and statistical analyses (wavelet coherence, trend tests, and mutation detection). B.T. prepared all figures and tables, and drafted the initial manuscript text. J.G. supervised the research, contributed to the interpretation of the meteorological results, revised the discussion, and provided methodological guidance. Both authors reviewed and approved the final manuscript.

Funding

The authors declare that no specific financial support was received for the research, authorship, and/or publication of this article. Open access funding for this article was provided by the University of Málaga under the transformative agreement with Springer Nature.

Acknowledgement

The authors express their gratitude to the National Institute of Meteorology and Hydrology (INAMHI) of Ecuador for providing the daily meteorological station data used in this study. The first author also thanks the University of Málaga for the academic support and institutional resources provided during the development of this research.

Data Availability

The meteorological datasets analyzed during the current study are publicly available from the National Institute of Meteorology and Hydrology (INAMHI) of Ecuador. Although the data are free of charge, access requires a formal request through INAMHI's official services portal at https://servicios.inamhi.gob.ec/. Additionally, the reference satellite precipitation data (CHIRPS) and reanalysis data (ERA5) used in the homogenization process are open-access and can be downloaded from the Climate Engine platform (https://www.climateengine.org/).

References

1. Aceituno P (1992) Anomalias de precipitacion en chile central relacionadas con la oscilacion del sur: mecanismos asociados. *Paleo ENSO Records International Symposium*, (March), 1–5
2. Aceituno P, Prieto MdelR, Solari ME, Martínez A, Poveda G, Falvey M (2009) The 1877–1878 El Niño episode: associated impacts in South America. Clim Change 92(3–4):389–416. https://doi.org/10.1007/s10584-008-9470-5
3. Alidoost F, Stein A, Su Z (2018) Copula-based interpolation methods for air temperature data using collocated covariates. Spat Stat 28:128–140. https://doi.org/10.1016/j.spasta.2018.08.003

4. Andreoli RV, Kayano MT (2005) ENSO-related rainfall anomalies in South America and associated circulation features during warm and cold Pacific decadal oscillation regimes. Int J Climatol 25(15):2017–2030. https://doi.org/10.1002/joc.1222
5. Arakawa O, Kitoh A (2004) Comparison of local precipitation–SST relationship between the observation and a reanalysis dataset. Geophys Res Lett 31(12). https://doi.org/10.1029/2004GL020283
6. Avila-Diaz A, Torres RR, Zuluaga CF, Cerón WL, Oliveira L, Benezoli V, Rivera IA, Marengo JA, Wilson AB, Medeiros F (2023) Current and Future Climate Extremes Over Latin America and Caribbean: Assessing Earth System Models from High Resolution Model Intercomparison Project (HighResMIP). Earth Syst Environ 7(1):99–130. https://doi.org/10.1007/s41748-022-00337-7
7. Ballari D, Giraldo R, Campozano L, Samaniego E (2018) Spatial functional data analysis for regionalizing precipitation seasonality and intensity in a sparsely monitored region: Unveiling the spatio-temporal dependencies of precipitation in Ecuador. Int J Climatol 38(8):3337–3354. https://doi.org/10.1002/joc.5504
8. Beck HE, Westra S, Tan J, Pappenberger F, Huffman GJ, McVicar TR, Gründemann GJ, Vergopolan N, Fowler HJ, Lewis E, Verbist K, Wood EF (2020) PPDIST, global 0.1° daily and 3-hourly precipitation probability distribution climatologies for 1979–2018. Sci Data 7(1):302. https://doi.org/10.1038/s41597-020-00631-x
9. Bendix A, Bendix J (2006) Heavy rainfall episodes in Ecuador during El Niño events and associated regional atmospheric circulation and SST patterns. Adv Geosci 6:43–49. https://doi.org/10.5194/adgeo-6-43-2006
10. Buytaert W, Celleri R, Willems P, Bièvre B, De, Wyseure G (2006) Spatial and temporal rainfall variability in mountainous areas: A case study from the south Ecuadorian Andes. J Hydrol 329(3–4):413–421. https://doi.org/10.1016/j.jhydrol.2006.02.031
11. Buytaert W, Deckers J, Wyseure G (2007) Regional variability of volcanic ash soils in south Ecuador: The relation with parent material, climate and land use. CATENA 70(2):143–154. https://doi.org/10.1016/j.catena.2006.08.003
12. Cai W, McPhaden MJ, Grimm AM, Rodrigues RR, Taschetto AS, Garreaud RD, Dewitte B, Poveda G, Ham Y-G, Santoso A, Ng B, Anderson W, Wang G, Geng T, Jo H-S, Marengo JA, Alves LM, Osman M, Li S, Vera C (2020) Climate impacts of the El Niño–Southern Oscillation on South America. Nat Reviews Earth Environ 1(4):215–231. https://doi.org/10.1038/s43017-020-0040-3
13. Cai W, Ng B, Wang G, Santoso A, Wu L, Yang K (2022) Increased ENSO sea surface temperature variability under four IPCC emission scenarios. Nat Clim Change 12(3):228–231. https://doi.org/10.1038/s41558-022-01282-z
14. Cerón WL, Kayano MT, Andreoli RV, Canchala T, Avila-Diaz A, Ribeiro IO, Rojas JD, Escobar-Carbonari D, Tapasco J (2024) New insights into trends of rainfall extremes in the Amazon basin through trend-empirical orthogonal function (1981–2021). Int J Climatol 44(11):3955–3975. https://doi.org/10.1002/joc.8561

15. Coll J, Domonkos P, Guijarro J, Curley M, Rustemeier E, Aguilar E, Walsh S, Sweeney J (2020) Application of homogenization methods for Ireland's monthly precipitation records: Comparison of break detection results. Int J Climatol 40(14):6169–6188. https://doi.org/10.1002/joc.6575
16. Di Leo N, Barbona I, Beltrán C, Forgioni FP, Coronel A, Jozami E (2024) Temporal variability of spatial patterns of correlations between summer rainfall and the Oceanic Niño Index in the Pampean region. Sci Total Environ 955:176849. https://doi.org/10.1016/j.scitotenv.2024.176849
17. Díaz D, Villegas N (2022) Wavelet coherence between ENSO indices and two precipitation databases for the Andes region of Colombia. Atmosfera 35(2):237–271. https://doi.org/10.20937/ATM.52890
18. Dijkstra HA (2006) The ENSO phenomenon: Theory and mechanisms. Adv Geosci 6:3–15. https://doi.org/10.5194/adgeo-6-3-2006
19. Espinoza Villar JC, Ronchail J, Guyot JL, Cochonneau G, Naziano F, Lavado W, De Oliveira E, Pombosa R, Vauchel P (2009) Spatio-temporal rainfall variability in the Amazon basin countries (Brazil, Peru, Bolivia, Colombia, and Ecuador). Int J Climatol 29(11):1574–1594. https://doi.org/10.1002/joc.1791
20. Gil Martínez C (2018) ANÁLISIS DE COMPONENTES PRINCIPALES (PCA). *RPubs by RStudio*. https://rpubs.com/Cristina_Gil/PCA
21. Gouhier T, Grinsted A, Simko V (2021) *biwavelet: Conduct Univariate and Bivariate Wavelet Analyses*. https://cran.r-project.org/web/packages/biwavelet/index.html
22. Grimm AM, Tedeschi RG (2009) ENSO and extreme rainfall events in South America. J Clim 22(7):1589–1609. https://doi.org/10.1175/2008JCLI2429.1
23. Grinsted A, Moore JC, Jevrejeva S (2004) Application of the cross wavelet transform and wavelet coherence to geophysical time series. Nonlinear Process Geophys 11(5/6):561–566. https://doi.org/10.5194/npg-11-561-2004
24. Guijarro JA, López JA, Aguilar E, Domonkos P, Venema VKC, Sigró J, Brunet M (2023) Homogenization of monthly series of temperature and precipitation: Benchmarking results of the MULTITEST project. Int J Climatol 43(9):3994–4012. https://doi.org/10.1002/joc.8069
25. Harris I, Osborn TJ, Jones P, Lister D (2020) Version 4 of the CRU TS monthly high-resolution gridded multivariate climate dataset. Sci Data 7(1):109. https://doi.org/10.1038/s41597-020-0453-3
26. He Z, Dai A, Vuille M (2021) The joint impacts of Atlantic and Pacific multidecadal variability on South American precipitation and temperature. J Clim 1–55. https://doi.org/10.1175/JCLI-D-21-0081.1
27. Ilbay-Yupa M, Casimiro L, Rau WS, Zubieta P, R., Castillón F (2021) Updating regionalization of precipitation in Ecuador. Theoret Appl Climatol 143(3–4):1513–1528. https://doi.org/10.1007/s00704-020-03476-x
28. Imfeld N, Sedlmeier K, Gubler S, Correa Marrou K, Davila CP, Huerta A, Lavado-Casimiro W, Rohrer M, Scherrer SC, Schwierz C (2021) A combined view on precipitation and temperature climatology and trends in the southern Andes of Peru. Int J Climatol 41(1):679–698. https://doi.org/10.1002/joc.6645

29. Kessabi R, Hanchane M, Guijarro JA, Krakauer NY, Addou R, Sadiki A, Belmahi M (2022) Homogenization and Trends Analysis of Monthly Precipitation Series in the Fez-Meknes Region, Morocco. Climate 10(5):64. https://doi.org/10.3390/cli10050064
30. Kiefer J, Karamperidou C (2019) High-Resolution Modeling of ENSO-Induced Precipitation in the Tropical Andes: Implications for Proxy Interpretation. Paleoceanography Paleoclimatology 34(2):217–236. https://doi.org/10.1029/2018PA003423
31. Lachenbruch PA (2014) McNemar Test. Wiley StatsRef: Statistics Reference Online. Wiley. https://doi.org/10.1002/9781118445112.stat04876
32. Laraque A, Ronchail J, Cochonneau G, Pombosa R, Guyot JL (2007) Heterogeneous Distribution of Rainfall and Discharge Regimes in the Ecuadorian Amazon Basin. J Hydrometeorol 8(6):1364–1381. https://doi.org/10.1175/2007JHM784.1
33. Liu Y, Liang S, X., Weisberg RH (2007) Rectification of the Bias in the Wavelet Power Spectrum. J Atmos Ocean Technol 24(12):2093–2102. https://doi.org/10.1175/2007JTECHO511.1
34. McNemar Q (1947) Note on the Sampling Error of the Difference Between Correlated Proportions or Percentages. Psychometrika 12(2):153–157. https://doi.org/10.1007/BF02295996
35. Ormaza-González FI, Martillo-Bustamante C, Espinoza E, Proust J-N, Michaud F, Lebrun J-F (2026) Disentangling Eastern Pacific Warming: El Niño 2023–2024 vs seasonal Panamá Bay influence. *Frontiers in Marine Science*, *12*. https://doi.org/10.3389/fmars.2025.1737039
36. Pembury Smith MQR, Ruxton GD (2020) Effective use of the McNemar test. Behav Ecol Sociobiol 74(11):133. https://doi.org/10.1007/s00265-020-02916-y
37. Rasmusson EM, Wang X, Ropelewski CF (1990) The biennial component of ENSO variability. J Mar Syst 1(1–2):71–96. https://doi.org/10.1016/0924-7963(90)90153-2
38. Reboita MS, Ambrizzi T, Crespo NM, Dutra LMM, Ferreira GW, de Rehbein S, Drumond A, da Rocha A, R. P., de Souza CA (2021) Impacts of teleconnection patterns on South America climate. Ann N Y Acad Sci 1504(1):116–153. https://doi.org/10.1111/nyas.14592
39. Rodríguez MD, Ariza ÁLG, Pérez AH, Mora MED (2018) Análisis de componentes principales. Introducción al Análisis Estadístico Multivariado Aplicado Experiencia y Casos En El Caribe Colombiano 29–51. https://doi.org/10.2307/j.ctvvn8c9.5
40. Rollenbeck RT, Fabian P, Bendix J (2006) Precipitation dynamics and chemical properties in tropical mountain forests of Ecuador. Adv Geosci 6:73–76. https://doi.org/10.5194/adgeo-6-73-2006
41. Rollenbeck RT, Orellana-Alvear J, Bendix J, Rodríguez Arisméndiz RA, Pucha-Cofrep F, Guallpa M, Fries A, Célleri R (2022) The Coastal El Niño Event of 2017 in Ecuador and Peru: A Weather Radar Analysis. Remote Sens 14(4). https://doi.org/10.3390/rs14040824
42. Rossel F, Cadier E (2009) El Niño and prediction of anomalous monthly rainfalls in Ecuador. Hydrol Process 23(22):3253–3260. https://doi.org/10.1002/hyp.7401
43. Santos F, Jara J, Acosta N, Galeas R, de Bièvre B (2025) Assessing Annual and Monthly Precipitation Anomalies in Ecuador Bioregions Using WorldClim CMIP6 GCM Ensemble Projections and Dynamic Time Warping. Int J Climatol 45(2). https://doi.org/10.1002/joc.8685

44. Stevenson S, Fox-Kemper B, Jochum M, Rajagopalan B, Yeager SG (2010) ENSO Model Validation Using Wavelet Probability Analysis. J Clim 23(20):5540–5547. https://doi.org/10.1175/2010JCLI3609.1
45. Thielen DR, Ramoni-Perazzi P, Zamora-Ledezma E, Puche ML, Marquez M, Quintero JI, Rojas W, Quintero A, Bianchi G, Soto-Werschitz IA, Arizapana-Almonacid MA (2023) Effect of extreme El Niño events on the precipitation of Ecuador. Nat Hazards Earth Syst Sci 23(4):1507–1527. https://doi.org/10.5194/nhess-23-1507-2023
46. Timmermann A, An S-I, Kug J-S, Jin F-F, Cai W, Capotondi A, Cobb KM, Lengaigne M, McPhaden MJ, Stuecker MF, Stein K, Wittenberg AT, Yun K-S, Bayr T, Chen H-C, Chikamoto Y, Dewitte B, Dommenget D, Grothe P, Zhang X (2018) El Niño–Southern Oscillation complexity. Nature 559(7715):535–545. https://doi.org/10.1038/s41586-018-0252-6
47. Tobar V, Wyseure G (2018) Seasonal rainfall patterns classification, relationship to ENSO and rainfall trends in Ecuador. Int J Climatol 38(4):1808–1819. https://doi.org/10.1002/joc.5297
48. Torrence C, Compo G (1998) *A Practical Guide to Wavelet Analysis*. *79*(1), 61–78. https://doi.org/https://doi.org/10.1175/1520-0477(1998)079%3C0061:APGTWA%3E2.0.CO;2
49. Tumbaco Vega BA, Solórzano Venegas MS, Valencia Castillo BG (2026) Impact of climate change on human occupation of the Ecuadorian Amazon over the past 4500 years. Antiquity 100(411):602–618. https://doi.org/10.15184/aqy.2026.10321
50. Valdez-Cepeda RD, Galván-Tejada CE, Galván-Tejada JI, Medina-García G, Blanco-Macías F, de Méndez-Gallegos S J., Magallanes-Quintanar R (2020) Relationship between precipitation anomalies and multivariate ENSO index through wavelet coherence analysis. Atmósfera. https://doi.org/10.20937/ATM.52541
51. Vargas D, Chimborazo O, László E, Temovski M, Palcsu L (2022) Rainwater Isotopic Composition in the Ecuadorian Andes and Amazon Reflects Cross-Equatorial Flow Seasonality. Water 14(13):2121. https://doi.org/10.3390/w14132121
52. Vilema-Escudero SF, Orellana MM, IN LOCAL HEALTH SERVICES IN ECUADOR; RIESGO CLIMÁTICO EN LOS SERVICIOS DE SALUD LOCAL EN ECUADOR (2024) CLIMATE RISK. Granja 40(2):37–49. https://doi.org/10.17163/lgr.n40.2024.02
53. Vuille M, Bradley RS, Keimig F (2000) Climate variability in the Andes of Ecuador and its relation to tropical Pacific and Atlantic Sea Surface temperature anomalies. J Clim 13(14):2520–2535. https://doi.org/10.1175/1520-0442(2000)013%3C2520:CVITAO%3E2.0.CO;2
54. Wang Y, Luo Y, Lu J, Liu F (2019) Changes in ENSO amplitude under climate warming and cooling. Clim Dyn 52(3–4):1871–1882. https://doi.org/10.1007/s00382-018-4224-1
55. Zhang Y, Liang C (2020) Analysis of Annual and Seasonal Precipitation Variation in the Qinba Mountain area, China. Sci Rep 10(1):961. https://doi.org/10.1038/s41598-020-57743-y

Figures

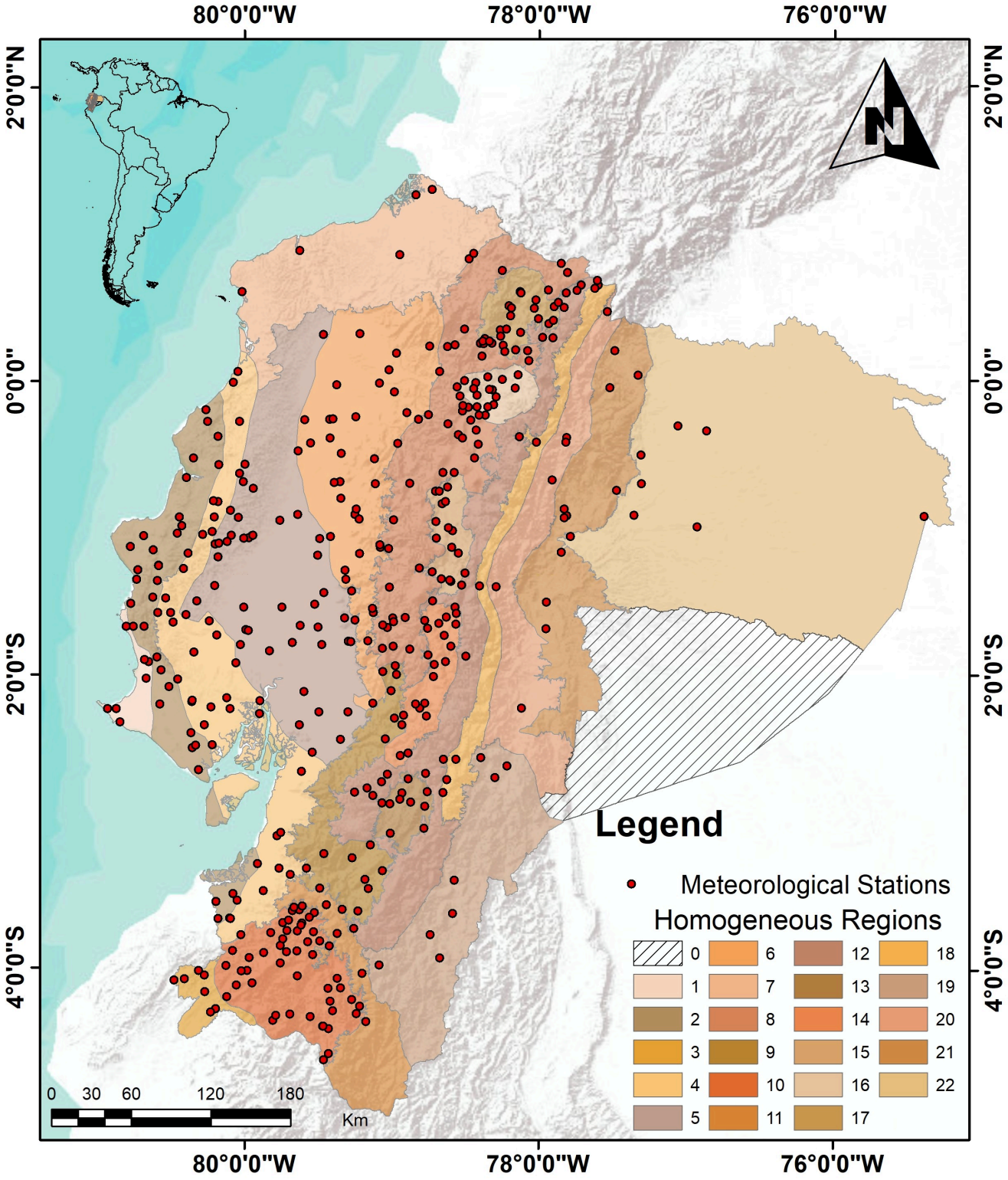


Figure 1

Spatial location of the 433 meteorological stations in the Ecuadorian continental territory and delimitation of the 22 homogeneous precipitation zones.

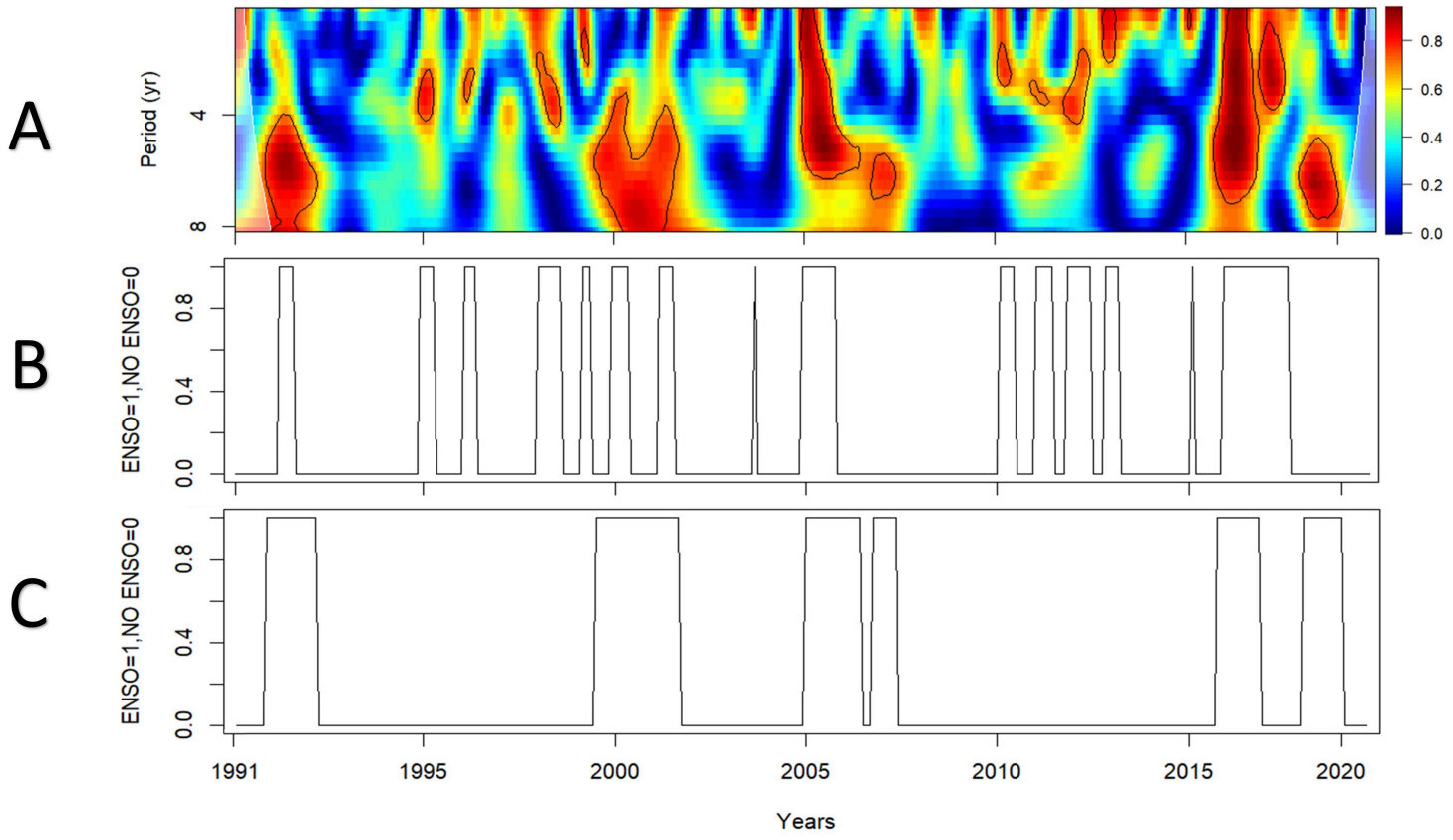


Figure 2

Result of the wavelet coherence analysis of regional precipitation (scaled PC1) against the Niño 1+2 index in a sample zone. A) Heatmap of spectral coherence in the time-frequency domain (black contours indicate significance at 95%). B) Presence (1) and absence (0) of the coherence signal in the high-frequency band (2-4 years). C) Presence (1) and absence (0) of the coherence signal in the low-frequency band (5-8 years).

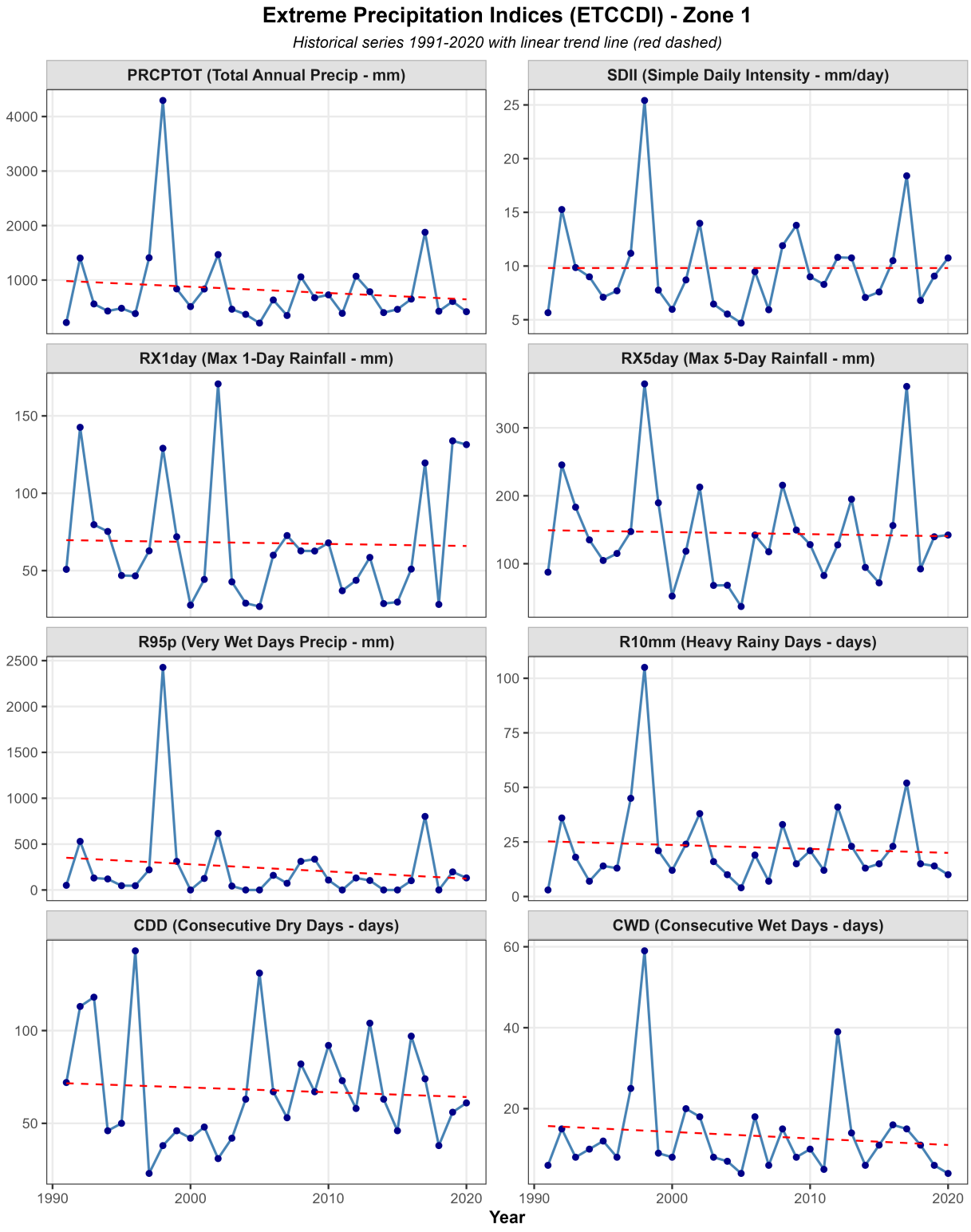


Figure 3

Historical time series (1991-2020) and sequential Mann-Kendall analysis for the eight extreme precipitation indices in a sample zone, showing annual trends (blue dots and lines, with a dashed red line for the linear trend) and direct (UF, blue line) and backward (UB, red line) curves for mutation detection, and their critical significance limits (dashed horizontal lines at ± 1.96).

Supplementary Files

This is a list of supplementary files associated with this preprint. Click to download.

- SupplementaryMaterial.docx